The composition and redox state of hydrous partial melts generated at the top of the lower mantle

Rong Huang[1], Tiziana Boffa Ballaran, Catherine A. McCammon, and Daniel J. Frost

Bayerisches Geoinstitut, Universität Bayreuth, D-95440 Bayreuth, Germany

Corresponding author: Rong Huang (Rong.Huang@ucl.ac.uk)

[1] Present address: Department of Earth Sciences, University College London, London, UK

Abstract:

Seismic low-velocity zones, that are proposed to form through hydrous partial melting, have been observed at the top of the lower mantle. The buoyancy of such melts will depend significantly on their iron content, but little is known about how iron partitions into melts under these conditions. In this study, ferrous and ferric iron partitioning between bridgmanite and melt has been studied at 25 GPa and 1973 K. Increasing oxygen fugacity and the Al content of bridgmanite can both change the mineral–melt partitioning of iron from incompatible to compatible. Hydrous partial melts at the top of a pyrolitic lower mantle are calculated to have an $Fe^{3+}/\sum Fe$ ratio of 0.26–0.5 and a total iron content of 5.9–7.8 wt.% in the f_{O_2} range between IW + 2 and IW + 4. Such melts would be less dense than the surrounding lower mantle and would migrate upwards into the transition zone. This could facilitate the formation of superdeep diamonds and crystallize an assemblage that also contains ferropericlase as the melts lose water to the surrounding ringwoodite.

Key words: Fe partitioning; bridgmanite; hydrous melt; oxygen fugacity; thermodynamic model; superdeep diamond

1. Introduction

Although partial melting of the mantle occurs principally in the upper mantle, there is evidence for melting within deeper layers of the interior (Garnero & McNamara, 2008; Garnero et al., 2016; Lay et al., 1998; Panero et al., 2020; Schmandt et al., 2014). Ultra-low velocity zones at the base of the lower mantle might result from partial melting within the thermal boundary layer at the core–mantle boundary (Berryman, 2000; Lay et al., 2004; Revenaugh & Meyer, 1997; Rost et al., 2005; Thorne & Garnero, 2004; Williams & Garnero, 1996) and a

number of studies have linked low shear wave velocities in the vicinity of the mantle transition zone to the presence of H_2O induced melting (Bercovici & Karato, 2003; Schmandt et al., 2014; Song et al., 2004; Toffelmier & Tyburczy, 2007). Beneath the 660 km seismic discontinuity, for example, slow seismic wave velocities have been proposed based on observations of seismic P-to-S conversions that could be interpreted as melt layers formed through dehydration as material is transported downwards out of the mantle transition zone (Liu et al., 2016; Liu et al., 2018; Schmandt et al., 2014). This would be consistent with a decrease in the amount of water that can be stored in mineral structures as material leaves the transition zone (Bolfan-Casanova et al., 2000; Inoue et al., 1995; Kohlstedt et al., 1996; Murakami et al., 2002; Smyth et al., 2003; Williams & Hemley, 2001). Water induced melting layers could potentially act as filters that influence the geochemical evolution of the mantle (Bercovici & Karato, 2003; Nakajima et al., 2019). An important aspect is the behavior of iron during such partial melting processes, which will largely control whether the melt could be neutrally buoyant in the mantle at a particular level and thus accumulate. Furthermore, the difference in partitioning between Fe^{2+} and Fe^{3+} can control how the redox state of the two resulting reservoirs will evolve (Amundsen & Neumann, 1992). Factors that control the partitioning of iron and the impact of redox state, however, are very poorly understood at lower mantle conditions.

When determined in ultramafic systems at conditions compatible with the top of the lower mantle, the apparent Fe–Mg exchange coefficient between bridgmanite (Brg) and melt, defined as,

$$K_{\mathrm{D}}(\mathrm{app}) = (x_{\mathrm{Fe}}/x_{\mathrm{Mg}})_{\mathrm{Brg}}/(x_{\mathrm{Fe}}/x_{\mathrm{Mg}})_{\mathrm{melt}} \quad (1)$$

where x_{Fe} is the mole fraction of all iron analyzed in the phases in question (i.e. ferric plus ferrous), has values ranging from approximately 0.5 to 0.2 (Corgne et al., 2005; Hirose & Fei, 2002; Ito et al., 2004; Ito & Takahashi, 1987; Kuwahara et al., 2018; Liebske et al., 2005; McFarlane et al., 1994; Trønnes et al., 1992; Trønnes & Frost, 2002). Here iron is assumed to

mix only on the Mg-site in a three-oxygen Brg formula unit, whereas for the melt all cations are assumed to mix on a single site. The recent hydrous partial melting experiments of Nakajima et al. (2019), however, report a significantly higher value of approximately 1.1, while similar experiments by Kawamoto (2004) report a value of approximately 0.7. Although some of these differences may arise from the effects of temperature, it is quite likely that changes in the redox state of iron also influence its partitioning. Although Fe^{3+} behaves more incompatibly than Fe^{2+} during basalt petrogenesis at upper mantle conditions (Canil et al., 1994; Davis & Cottrell, 2018; Mallmann & O'Neill, 2009; Sorbadere et al., 2018), its behavior at higher pressures is completely unknown, but could have an important influence on melt density.

In this study, we have investigated iron partitioning between Brg, ferropericlase (Fp) and coexisting hydrous melt at 25 GPa and 1973 K using a multi-anvil apparatus and determined the $Fe^{3+}/\sum Fe$ ratios of coexisting Brg and melt using Mössbauer spectroscopy. Hydrous ultramafic starting materials were employed and the experimental oxygen fugacity (fO_2) was monitored using an Ir–Fe alloy redox sensor (Stagno & Frost, 2010). Based on the results and subsequent thermodynamic modelling, the composition of hydrous melts beneath the 660 km discontinuity are calculated and their iron contents are determined as a function of bulk composition and fO_2. We examine the consequences for the buoyancy of partial melt layers and the implications for the formation of superdeep diamonds and their inclusions.

2. Experiments

Glass with the nominal composition $Mg_{0.93}Fe_{0.07}Si_{0.93}Al_{0.07}O_3$ (En93) was synthesized by melting dried reagent grade oxide mixtures of MgO, Al_2O_3, SiO_2 and Fe_2O_3 at 1650 ˚C in a 1 atmosphere furnace followed by rapid quenching in water. The glass was then reduced in a CO_2–CO gas-mixing furnace at 1250 ˚C for 48 hours at an fO_2 of 1 log unit above the iron–wüstite buffer (IW). Mössbauer spectroscopy confirmed the presence of only Fe^{2+} in the

recovered pyroxene. The pyroxene was then mixed with 5 wt.% $(Mg_{0.9}Fe_{0.1})O$ and 15 wt.% Fe metal to buffer the fO_2, and in most experiments 5 wt.% Ir (Table 1) was added to monitor the fO_2. Approximately 5–20 wt.% water was also added to the starting material either using a syringe as free H_2O or as $Mg(OH)_2$ (Table 1).

Table 1 Starting compositions and run products.

Run No.	Start composition (wt.%)	Recovered assemblages
S6813	80% En93, 15% Fe, 5% $(Mg_{0.9}Fe_{0.1})O$, 0.1 μl H_2O	Brg + Fp + melt
S6833	75% En93, 15% Fe, 5% Ir, 5% $(Mg_{0.9}Fe_{0.1})O$, 0.4 μl H_2O	Brg + Fp + Fe–Ir + melt
S6840	75% En93, 15% Fe, 5% Ir, 5% $(Mg_{0.9}Fe_{0.1})O$, 0.4 μl H_2O	Brg + Fp + Fe–Ir + melt
S6843	75% En93, 15% Fe, 5% Ir, 5% $(Mg_{0.9}Fe_{0.1})O$, 0.2 μl H_2O	Brg + Fp + Fe–Ir + melt
S6848	63.8% En93, 15% Fe, 5% Ir, 16.2% $Mg(OH)_2$	Brg + Fp + Fe–Ir + melt

Notes: Brg = bridgmanite; Fp = ferropericlase; Fe–Ir = Fe–Ir metal alloys.

The starting compositions (Table 1) were loaded into gold foil capsules of 1.8 mm in length and 0.8 mm in diameter that were then placed inside platinum tubes of 2 mm in length and 1.0 mm in diameter, which were welded closed at each end. Each capsule was put into an MgO sleeve within a $LaCrO_3$ furnace in a 7 mm edge length Cr_2O_3-doped MgO octahedra and compressed to ~25 GPa using a 1200 tonne Kawai-type multi-anvil apparatus. Tungsten carbide anvils of 3 mm truncation edge length were used. After compression to the target pressure, the assembly was heated to 1973 K for 12 h and then quenched by turning off the electrical power. The pressure was released over 20 hours. Pressure calibrations are reported by Keppler and Frost (2005) and temperature was estimated from the electrical power using previous calibrations where type D thermocouple was employed (Huang et al., 2021).

Phase identification and textural observations of the run products were performed by means of microfocus X-ray diffraction and scanning electron microscopy. Chemical compositions were analyzed with an electron probe microanalyzer (EPMA) and the $Fe^{3+}/\sum Fe$

92 ratios of Brg and quenched melt regions were measured by Mössbauer spectroscopy (see Text
93 S1 and S2 for details).

94 # 3. Results

95 ## *3.1 Phase assemblages*

96 The recovered phase assemblages and chemical analyses are reported in Table 1 and 2,
97 respectively. All recovered samples contained Brg, Fp and quenched microcrystals from the
98 melt (Table 1). Brg coexists with quenched melt in the central part of the capsule (i.e. in the
99 highest temperature region) while Fp frequently crystallized towards the colder end (Fig. S1a).
100 Interstitial melt is also present around coexisting Brg and Fp crystals, however, indicating
101 cotectic phase relations. Ir metal in the starting material became an alloy with Fe (Table 3).

Table 2 Phase compositions in wt.% measured by EPMA and cation proportions normalized to total cations. All Fe (ΣFe) is treated as FeO. No. is the number of points measured for each phase and the number in parentheses is 1 standard deviation.

.	Phases	No.	MgO	SiO_2	FeO	Al_2O_3	Total	Mg	Si	Fe	Al	ΣCations
S6813	Brg	41	32.8(5)	52.7(5)	11.0(5)	3.4(2)	99.9(7)	0.852(8)	0.919(9)	0.160(6)	0.069(3)	2.00
	Fp	17	33.7(7)	0.13(7)	66.7(8)	0.13(4)	100.6(9)	0.472(6)	0.001 (1)	0.525(6)	0.0012(4)	1.00
	Melt	14	26.0(11)	23.3(20)	28.1(23)	1.5(4)	78.9(37)	0.445(26)	0.266(15)	0.269(17)	0.020(5)	1.00
S6833	Brg	61	33.0(3)	53.2(3)	10.6(4)	3.3(2)	100.2(7)	0.854(5)	0.924(6)	0.155(6)	0.067(3)	2.00
	Fp	7	35.8(3)	0.14(4)	65.0(11)	0.12(2)	101.0(13)	0.494(3)	0.0013(4)	0.503(4)	0.0013(2)	2.00
	Melt	99	27.4(13)	22.9(20)	28.9(20)	1.6(4)	80.7(31)	0.455(18)	0.255(19)	0.269(15)	0.021(5)	2.00
S6840	Brg	23	33.1(2)	52.2(4)	10.5(4)	3.2(2)	99.0(6)	0.866(4)	0.914(8)	0.154(6)	0.067(4)	2.00
	Fp	22	33.3(4)	0.10(4)	67.5(6)	0.10(3)	101.1(6)	0.467(5)	0.0009(3)	0.531(4)	0.0011(4)	1.00
	Melt	28	28.6(13)	21.7(14)	27.5(24)	1.6(1)	79.4(18)	0.478(23)	0.243(15)	0.257(22)	0.022(2)	1.00
S6843	Brg	32	33.1(4)	53.1(4)	10.5(5)	3.3(2)	99.9(8)	0.858(6)	0.923(6)	0.152(6)	0.067(4)	2.00
	Fp	18	31.3(3)	0.05(3)	69.0(9)	0.09(3)	100.4(9)	0.446(4)	0.0005(3)	0.552(4)	0.0010(4)	1.00
	Melt	6	28.3(11)	22.4(25)	27.2(40)	1.9(2)	79.2(22)	0.471(19)	0.250(28)	0.254(37)	0.026(2)	1.00
S6848	Brg	22	33.3(4)	54.0(4)	10.1(5)	3.3(2)	100.7(6)	0.857(8)	0.931(6)	0.145(7)	0.067(5)	2.00
	Fp	17	40.9(3)	0.06(3)	59.6(8)	0.10(3)	100.7(9)	0.549(4)	0.0005(3)	0.449(4)	0.0011(3)	1.00
	Melt	5	31.8(11)	21.2(16)	27.7(31)	1.5(8)	82.3(35)	0.506(17)	0.227(17)	0.248(27)	0.019(11)	1.00

105 The mineral compositions are relatively homogeneous throughout the capsule and no
106 chemical zoning was observed (Table 2), implying that compositions reached equilibrium
107 likely due to recrystallisation in the presence of the melt layer. The fine dendritic quenched
108 crystals of the hydrous melt (Fig. S1b) mainly consist of Fp, Phase D and ringwoodite (Rw)
109 based on X-ray diffraction. The presence of Rw implies a drop in pressure on quenching, which
110 has been reported previously (Armstrong et al., 2019). The low totals of the EPMA analyses
111 of 79–82 wt.% (Table 2) can be attributed to H_2O in phase D and fluid loss from the quenched
112 melt which leaves pores.

113 *3.2 Phase compositions and element partitioning*

114 In Fig. 1a, the (Mg+Fe)/Si ratio of the resulting melt is plotted against temperature
115 together with previous studies in hydrous (Nakajima et al., 2019) and dry peridotite systems
116 (Corgne et al., 2005; Hirose & Fei, 2002; Kuwahara et al., 2018; Liebske et al., 2005; Trønnes
117 & Frost, 2002) at similar pressure conditions. In these experiments, where both Brg and Fp
118 coexist along a cotectic, the (Mg+Fe)/Si ratio of the melt follows a near linear negative
119 relationship with temperature. Although some of the partial melts produced from chondritic
120 compositions (Liebske et al., 2005; Trønnes, 2000; Trønnes et al., 1992) are much more Fe-
121 rich (Fe/[Mg+Fe] = 0.5 – 0.6) than peridotite compositions (Fe/[Mg+Fe] = ~0.1), their
122 (Mg+Fe)/Si ratios are only very slightly higher (black triangles in Fig. 1a). Moreover, an
123 experiment saturated with Fe metal (the lower black circle in Fig.1a, Liebske et al., 2005)
124 shows a similar melt (Mg+Fe)/Si ratio to other experiments conducted in Re capsules, implying
125 very little, if any, dependence of melt (Mg+Fe)/Si ratio on Fe content or f_{O_2}. A hydrous partial
126 melt produced at the top of the lower mantle at a temperature < 2000 K would, therefore, be
127 MgO-rich with a (Mg+Fe)/Si ratio > 2.5 (Fig. 1a).

128

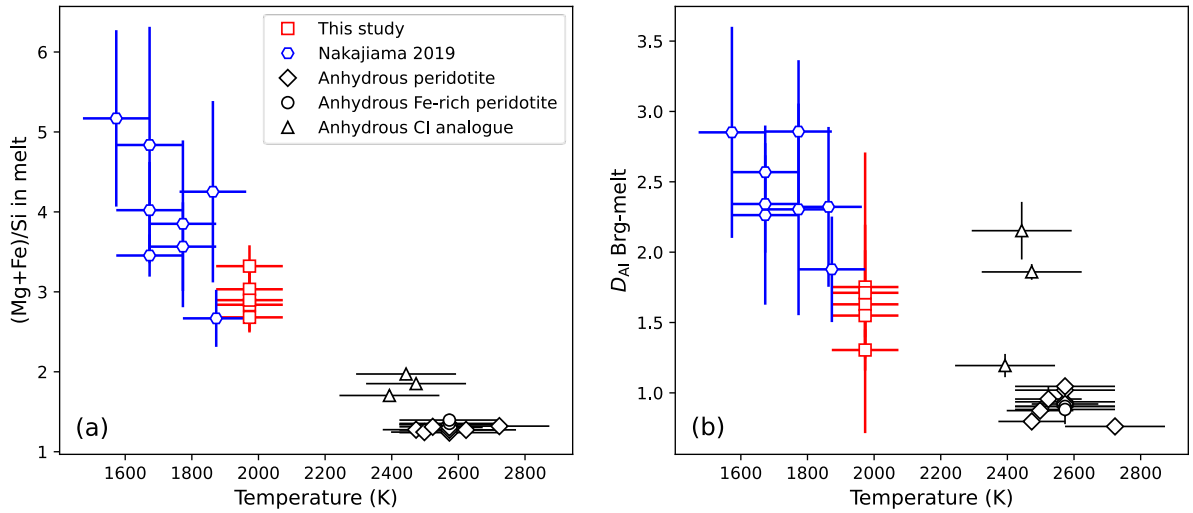

Fig. 1. (a) The (Mg+Fe)/Si ratio in the melt and (b) Al molar partition coefficient between Brg and melt as a function of synthesis temperature at 23.5–27 GPa in this study and previous studies of H_2O-saturated peridotite (Nakajima et al., 2019), dry peridotite (Corgne et al., 2005; Hirose & Fei, 2002; Kuwahara et al., 2018; Liebske et al., 2005; Trønnes & Frost, 2002) and CI chondrite analogue systems (Liebske et al., 2005; Trønnes, 2000; Trønnes et al., 1992).

The Al content of Brg in this study, 0.067(1) atoms per formula unit (pfu), is close to that in the starting pyroxene. The average molar partition coefficient of Al between Brg and melt ($D_{\mathrm{Al}}^{\mathrm{Brg/melt}} = x_{\mathrm{Al}}^{\mathrm{Brg}}/x_{\mathrm{Al}}^{\mathrm{melt}}$) is 1.6(2) in this study, where x_{Al} is the Al fraction of total cations in the corresponding phases, and lies between those of Nakajima et al. (2019) at lower temperatures and anhydrous peridotite studies at higher temperatures (Corgne et al., 2005; Hirose & Fei, 2002; Kuwahara et al., 2018; Liebske et al., 2005; Trønnes & Frost, 2002) (Fig. 1b). The anhydrous experiments show a constant $D_{\mathrm{Al}}^{\mathrm{Brg/melt}}$ of 0.90(8) for Brg Al contents varying from 0.04–0.13 pfu (Fig. 1b), i.e., in agreement with Henry's law. $D_{\mathrm{Al}}^{\mathrm{Brg/melt}}$ from chondritic systems are more scattered (black triangles in Fig. 1b) and more studies are needed to clarify why these differences arise for more Si and Fe rich bulk compositions.

The Fe/(Mg+Fe) ratios of phases from this study are higher than those of the starting material due to the oxidation of Fe metal by reaction with H_2O (Table 2). The Brg–melt K_D (app) and Fp–melt K_D (app) from this and previous studies are plotted against the Fe/(Mg+Fe)

ratio of Brg and Fp in Fig. 2. Even though the experimental conditions of Nakajima et al. (2019) overlap with those from the current study, the Brg–melt K_D (app) values are much higher than both this study and previous anhydrous experiments (Fig. 2a) and conversely, the Fp–melt K_D (app) values are much lower (Fig. 2b). This can only be attributed to the differences in redox state of the experiments. The starting material employed by Nakajima et al. (2019) contained only ferric iron and the presence of H_2O and the use of Pt capsules by Nakajima et al. (2019) should have ensured that most of the iron remained in the ferric state (McCammon et al., 2004). Using the recent model of Huang et al. (2021), it is possible to estimate the f_{O_2} for the experiments of Nakajima et al. (2019) as IW + 7(1), based on the reported total Fe and Al contents of Brg and the Fe content of coexisting Fp. The calculated $Fe^{3+}/\sum Fe$ ratio of Brg for these conditions is 0.95(1). The uncertainties are estimated from the uncertainties of Fe and Al content in Brg and Fe content in Fp reported in the study of Nakajima et al. (2019).

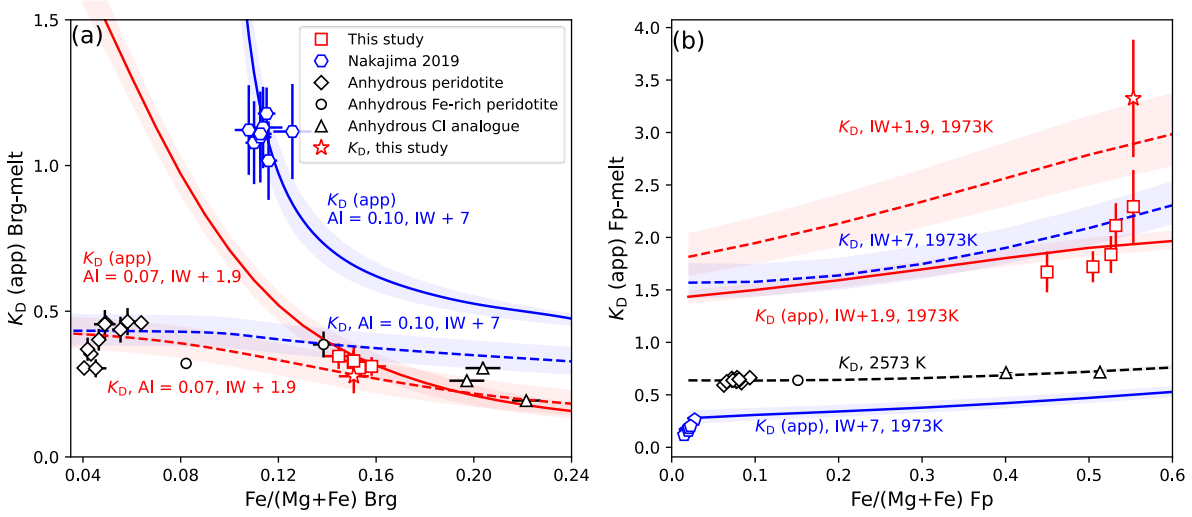

Fig. 2. The apparent Fe–Mg distribution coefficient, K_D (app), for (a) Brg and (b) Fp and melt versus the Fe/(Mg+Fe) ratio at ~25 GPa. Symbols indicate experimental results from this study (red square) and from H_2O-bearing peridotite (Nakajima et al., 2019, blue hexagons), dry peridotite (Corgne et al., 2005; Hirose & Fei, 2002; Kuwahara et al., 2018; Liebske et al., 2005; Trønnes & Frost, 2002, black diamonds and circles) and CI chondrite analogue compositions (Liebske et al., 2005; Trønnes, 2000; Trønnes et al., 1992, black triangles). The anhydrous experiments were performed at a higher temperature of ~ 2573 K. The red star is the actual K_D value of experiment S6840. Error bars are the 1σ

standard deviation. Model calculation results for K_D (app) and K_D as discussed in Section 4 are shown as solid and dashed curves respectively. (a) The calculation was performed with 0.07 pfu Al in Brg at f_{O_2} of IW + 1.9 (red curves) and with 0.10 pfu Al in Brg at IW + 7 (blue curves). (b) The calculation was performed at constant f_{O_2} of IW + 1.9 (red curves) and IW + 7 (blue curves). The black curve shows the model calculation at 2573 K.

For three of our experiments, the $Fe^{3+}/\sum Fe$ ratios of Brg were measured by Mössbauer spectroscopy and the fitting results reveal values of 0.42(7), 0.44(7) and 0.54(7) for S6840, S6843 and S6848 respectively (Table 3, Text S2, Fig. S2). The presence of Ir metal in four of our experiments (S6833, S6840, S6843 and S6848) also allowed the f_{O_2} of the experiments to be determined (Text S3) and a consistent f_{O_2} of IW + 1.9 (1) was obtained for all the four experiments (Table 3). Based on the similarity in experimental method, sample S6813 almost certainly experienced a very similar f_{O_2} even though no Ir was added in the starting material. Using these f_{O_2} values and the measured bulk Fe and Al contents of Brg, the $Fe^{3+}/\sum Fe$ ratios of Brg can be calculated with the model of Huang et al. (2021) and are found to be in excellent agreement with the Mössbauer measurements (Table 3), even though these data were not used to parameterize this model.

Table 3 Composition of the phases and the measured oxygen fugacity.

Run No.	X_{FeO} Fp	X_{Fe} alloy	log f_{O_2} (ΔIW)	$Fe^{3+}/\sum Fe$ Brg	$Fe^{3+}/\sum Fe$ melt	$Fe^{3+}/\sum Fe$ Brg[a]	$Fe^{3+}/\sum Fe$ melt[b]
S6813	0.525(6)	-	-	-	-	0.434	0.323
S6833	0.503(4)	0.24	1.99(18)	-	-	0.439	0.332
S6840	0.531(4)	0.29(2)	1.77(16)	0.42(7)	0.31(5)	0.435	0.310
S6843	0.552(4)	0.27(1)	1.90(14)	0.44(7)	-	0.444	0.320
S6848	0.449(4)	0.26(2)	1.81(18)	0.47(8)	-	0.459	0.302

[a] $Fe^{3+}/\Sigma Fe$ ratios of Brg calculated with the thermodynamic model by Huang et al. (2021) using the measured bulk Fe and Al content in Brg and the experimental f_{O_2} for each sample. [b] $Fe^{3+}/\Sigma Fe$ ratios of melt calculated with the thermodynamic model developed in this study using the measured bulk Fe and Al content in Brg and the experimental f_{O_2} for each sample. The f_{O_2} in S6813 was not measured and the average value of other experiments (IW + 1.9) was assumed.

191 The $Fe^{3+}/\sum Fe$ ratio of the quenched melt was also measured by Mössbauer spectroscopy
192 in one experiment (S6840) (Fig. S2b). Combined with the results from X-ray diffraction
193 refinement, an $Fe^{3+}/\sum Fe$ ratio of 0.31(5) was obtained for the quenched crystals (see Text S2
194 for details). In the absence of an obvious redox reaction that might occur on quenching, we
195 assume that the bulk $Fe^{3+}/\sum Fe$ ratio determined for the quenched assemblage of phases using
196 Mössbauer spectroscopy is the same as that of the melt.

197 # 4. Thermodynamic Modelling

198 *4.1 Fe-Mg partitioning between Brg and melt*

199 To explain the variation in Fe–Mg K_D (app) between Brg and melt seen in different studies
200 we need to be able to calculate the Fe^{3+}/Fe^{2+} ratio of Brg and melt and the Fe^{2+}–Mg exchange
201 between Brg and melt as a function of composition and fO_2. We can do this by considering
202 several mineral–melt equilibria. The exchange of Fe^{2+} and Mg between Brg and melt can be
203 expressed by:

204 $$\underset{\text{melt}}{FeO} + \underset{\text{Brg}}{MgSiO_3} = \underset{\text{melt}}{MgO} + \underset{\text{Brg}}{FeSiO_3} \quad (2)$$

206 At equilibrium, the Fe^{2+}–Mg Brg–melt exchange coefficient K_D, i.e. considering only the
207 determined Fe^{2+} content, can be described by:

208 $$R\mathit{T}\ln K_D = R\mathit{T}\ln\frac{x_{MgO}^{melt}x_{FeSiO_3}^{Brg}}{x_{FeO}^{melt}x_{MgSiO_3}^{Brg}} = -\Delta G_{P,T\,(2)}^{0} - R\mathit{T}\ln\frac{\gamma_{MgO}^{melt}\gamma_{FeSiO_3}^{Brg}}{\gamma_{FeO}^{melt}\gamma_{MgSiO_3}^{Brg}} \quad (3)$$

209 where $\Delta G_{P,T(2)}^{0}$ is the standard state Gibbs free energy change of Eq. (2) at the pressure and
210 temperature of interest, x_i^j is the molar fraction of component *i* in the particular site in phase *j*
211 where mixing is occurring and γ_{FeO}^{melt} is, for example, the activity coefficient of FeO in the

212 silicate melt. For the melt we consider single site mixing of all cations. The activity coefficient
213 expressions for each component can be described using a symmetric interaction expression e.g.,

214 $$R T \ln \gamma_{MgO}^{melt} = W_{Fe^{2+}Mg}^{melt} \left(1 - x_{MgO}^{melt}\right)^2 \quad (4)$$

215 $$R T \ln \gamma_{FeO}^{melt} = W_{Fe^{2+}Mg}^{melt} \left(1 - x_{FeO}^{melt}\right)^2 \quad (5)$$

216 where $W_{Fe^{2+}Mg}^{melt}$ is a Margules parameter describing the interaction energy of Fe^{2+}–Mg mixing
217 in the melt, with similar expressions used for Brg. Substituting Eq. (4) and (5) and their Brg
218 equivalents into Eq. (3) and rearranging gives the expression:

219 $$R T \ln K_D = -\Delta G_{P,T\,(2)}^0 - W_{Fe^{2+}Mg}^{melt} \left(1 - x_{MgO}^{melt}\right)^2 + W_{Fe^{2+}Mg}^{melt} \left(1 - x_{FeO}^{melt}\right)^2$$

220 $$- W_{Fe^{2+}Mg}^{Brg} \left(1 - x_{FeSiO_3}^{Brg}\right)^2 + W_{Fe^{2+}Mg}^{Brg} \left(1 - x_{MgSiO_3}^{Brg}\right)^2 \quad (6)$$

221 The value $W_{Fe^{2+}Mg}^{Brg}$ = - 4.9(76) kJ/mol can be taken directly from Nakajima et al. (2012).
222 $W_{Fe^{2+}Mg}^{melt}$ at such pressure conditions has not been reported but can be estimated by fitting Fe–
223 Mg partitioning data between Fp and melt in previous anhydrous experiments collected over a
224 range of Fe contents which yields values of 12.5(7) kJ/mol (black symbol and curve in Fig. 2b,
225 see Text S4 for details). By substituting the composition of experiment S6840, whose $Fe^{3+}/\sum Fe$
226 ratios of both Brg and melt were measured, into Eq. (6), $\Delta G_{25\ GPa,1973\ K\,(2)}^0$ = 30.1 (27) kJ/mol
227 can be obtained, where the uncertainties mainly come from the errors on the $Fe^{3+}/\sum Fe$
228 measurements.

229 A separate relationship is then used to describe the ferrous and ferric iron content of the
230 melt as a function of f_{O_2} using the melt–component equilibrium:

231 $$FeO + 1/4 O_2 = FeO_{1.5} \quad (7)$$

232 The standard state Gibbs free energy change for reaction (7) is:

$$-\Delta G^{0}_{P,T\,(7)} = \mathrm{R}T\ln\frac{x^{\mathrm{melt}}_{\mathrm{FeO_{1.5}}}}{(f_{\mathrm{O_2}})^{1/4}x^{\mathrm{melt}}_{\mathrm{FeO}}} + \mathrm{R}T\ln\frac{\gamma^{\mathrm{melt}}_{\mathrm{FeO_{1.5}}}}{\gamma^{\mathrm{melt}}_{\mathrm{FeO}}} \quad (8)$$

The effects of non-ideal interactions in the silicate melt can be estimated using previously determined interaction parameters (Jayasuriya et al., 2004) and the expression,

$$\ln\frac{\gamma_{\mathrm{FeO_{1.5}}}}{\gamma_{\mathrm{FeO}}} = 2248\frac{x_{\mathrm{MgO}}}{T} + 6278\frac{x_{\mathrm{AlO_{1.5}}}}{T} - 6680\left(\frac{x_{\mathrm{FeO}} - x_{\mathrm{FeO_{1.5}}}}{T}\right) \quad (9)$$

where x_i is the mole fraction of component i in the melt. Using the measured composition (Table 2) and $Fe^{3+}/\sum Fe$ (Table 3) of the melt in experiment S6840, together with the f_{O_2} determined for the experiment (Text S3, Table 3), $\Delta G^{0}_{25\ \mathrm{GPa},1973\ \mathrm{K}\,(7)}$=14.6(53) kJ/mol can be calculated from Eq. (8) and the uncertainty is propagated from the uncertainties of the composition and $Fe^{3+}/\sum Fe$ measurement.

The model of Huang et al. (2021) can then be used to calculate the Fe^{3+} and Fe^{2+} content of Brg for a given bulk composition and f_{O_2}. Using Eq. (3) the Fe^{2+} of the coexisting melt can be determined at the same conditions and with Eq. (8) the melt Fe^{3+} content can be determined using estimates for the other redox independent melt components from the experimental analyses. Together with the constraints of melt (Mg+Fe)/Si ratio and $D^{\mathrm{Brg/melt}}_{\mathrm{Al}}$ as discussed in Section 3, these data can be used to calculate the K_D (app) and actual K_D between Brg and melt as a function of composition and f_{O_2} at 25 GPa and 1973 K. In Fig. 2a, the calculation results of K_D (app) performed at IW + 1.9 with fixed Brg Al content of 0.07 pfu (similar to our experiments) and at IW + 7 with fixed Brg Al content of 0.10 pfu (similar to experiments of Nakajima et al., 2019) as a function of the Fe/(Fe+Mg) ratio of Brg are shown as solid curves, which are consistent not only with our experiments, on which the model is based, but also with the data of Nakajima et al. (2019), which were not used to constrain the model. The large difference of K_D (app) among different studies can be well explained by the difference in Al content and f_{O_2} of the experiments, which are the two main factors controlling the $Fe^{3+}/\sum Fe$

ratios in Brg. The actual K_D, i.e. involving only Fe^{2+}–Mg exchange, at corresponding conditions was also calculated and shown in Fig. 2a as dashed curves.

4.2 Fe-Mg partitioning between Fp and melt

Using the models described above and the experimentally determined f_{O_2} and total Fe and Al contents of Brg, the $Fe^{3+}/\sum Fe$ ratios of melts in this study can be calculated and are listed in Table 3, where they can be seen to be very similar to sample S6840 where the $Fe^{3+}/\sum Fe$ ratio was actually measured. Substituting the measured compositions of Fp and melt in the experiments into Eq. (S10) (given in the supplementary information), we obtain $\Delta G^0_{25\ \mathrm{GPa},1973\ \mathrm{K}\ (\mathrm{S5})} = -11.6(12)$ kJ/mol for the Fe^{2+}–Mg exchange reaction between Fp and melt (Eq. (S5)). By incorporating this into the model, the K_D (app) and K_D between Fp and melt can be calculated as a function of composition and f_{O_2} at 25 GPa and 1973 K. The calculation results performed at constant f_{O_2} of IW + 1.9 (similar to our experiments) and IW + 7 (similar to experiments of Nakajima et al., 2019) are plotted against the Fe/(Fe+Mg) ratio of Fp as red and blue curves respectively in Fig. 2b. The model results agree with both our data and those of Nakajima et al. (2019) well and show that f_{O_2} also plays an important role in Fe–Mg K_D (app) between Fp and melt.

4.3 Oxygen fugacity dependence

In Fig. 3, K_D (app), the actual K_D and the (mass) partition coefficients between Brg and melt are calculated as a function of f_{O_2}. For the Brg composition found in this study (compo. B in Fig. 3), K_D (app) and the (mass) partition coefficients for total Fe ($D_{\mathrm{Fe}}^{\mathrm{Brg/melt}}$) and Fe^{3+} ($D_{\mathrm{Fe_2O_3}}^{\mathrm{Brg/melt}}$) are not predicted to change significantly with f_{O_2}. The experimentally determined $D_{\mathrm{Fe}}^{\mathrm{Brg/melt}}$ and $D_{\mathrm{Fe_2O_3}}^{\mathrm{Brg/melt}}$ are 0.38(4) and 0.5(1) respectively, indicating that both are moderately incompatible in Brg.

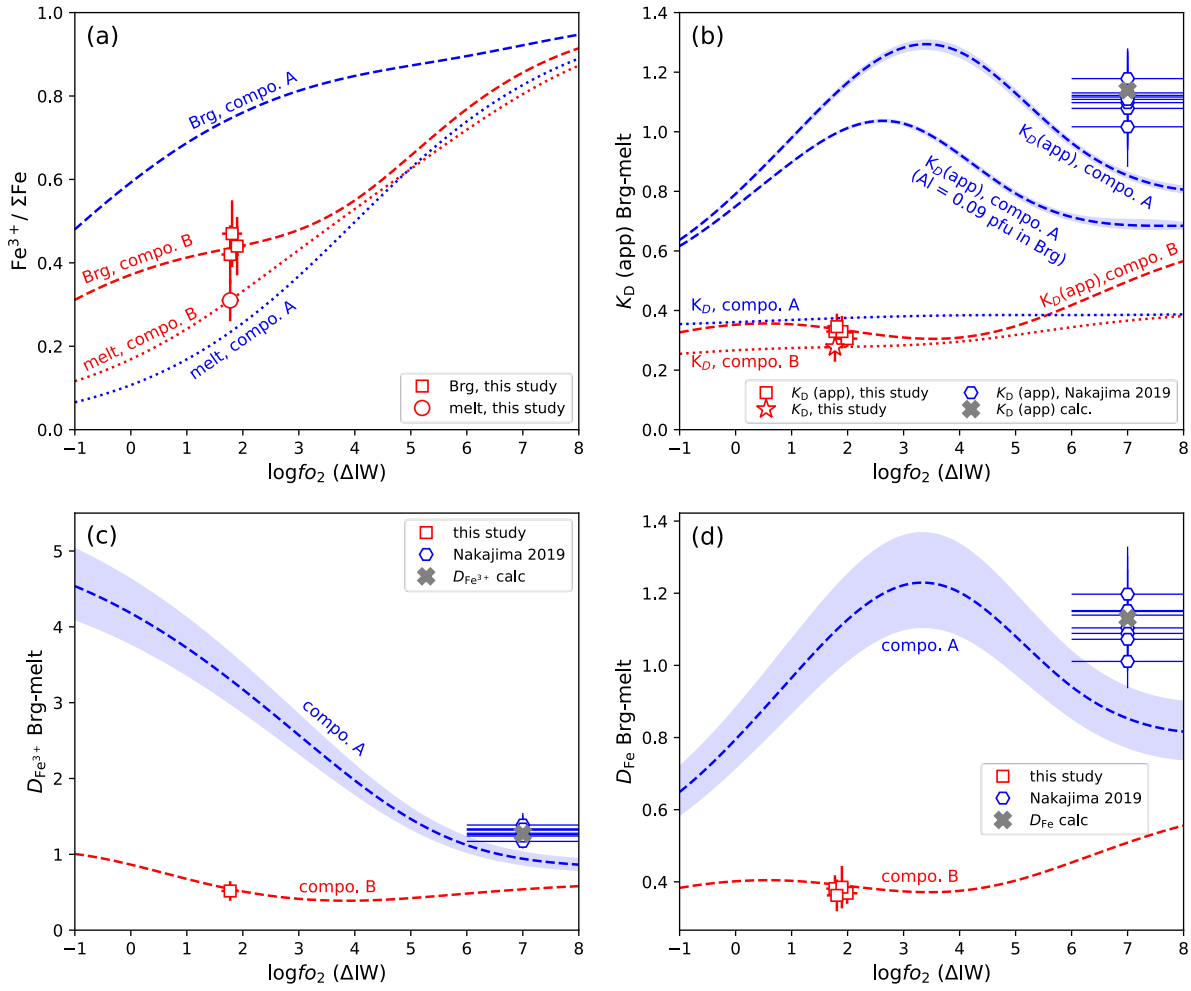

Fig. 3. Experimental values and model calculation results for (a) $Fe^{3+}/\sum Fe$ ratio; (b) apparent Fe–Mg distribution coefficient K_D (app); (c) mass partition coefficients for Fe^{3+} ($D^{Brg/melt}_{Fe_2O_3}$) and (d) total Fe ($D^{Brg/melt}_{FeO+Fe_2O_3}$) between Brg and melt as a function of f_{O_2}. Red curves indicate calculations with the same Al and Fe content of Brg and melt water content as in the current study (compo. B), which is lower and higher respectively than Brg in a pyrolitic bulk composition (compo. A), shown by blue curves. The calculation uncertainties arising from different melt fraction and H_2O content assumptions are shown as shaded areas. The grey cross shows the model calculation using the same bulk composition as in Nakajima et al. (2019). Experimental data from Nakajima et al. (2019) are in good agreement with our calculations, although they were not used in the thermodynamic modelling. In (b), the actual K_D between Brg and melt is also calculated and shown as dotted curves. An additional calculation with a lower Brg Al content of 0.09 pfu is also shown. In (c), the $Fe^{3+}/\sum Fe$ ratios for the experimental data of Nakajima et al. (2019) are estimated for Brg and melt using the models of Huang et al. (2021) and this study, respectively.

Using the derived model, we can also attempt to estimate the ferric and ferrous iron content expected for a hydrous partial melt at the top of the lower mantle, as proposed in the study of Schmandt et al. (2014). Based on a pyrolitic mantle composition employed by Irifune (1994), we perform a mass balance calculation to determine the composition of the partial melt and employ the thermodynamic melt relations described above along with the model of Huang et al. (2021) to determine the Brg and Fp compositions. We perform the calculation at a typical adiabatic temperature (Katsura et al., 2010) for this depth of 1973 K and assume a melt (Mg+Fe)/Si ratio of 2.96 and $D_{\mathrm{Al}}^{\mathrm{Brg/melt}}$ of 1.6 determined at this temperature from Fig. 1. Small amounts of Al in Fp and $CaSiO_3$ perovskite (Irifune, 1994) are neglected, as are the concentrations of Cr, Na and Ti. The melt CaO content (9 wt.%) from Nakajima et al. (2019) is employed. Due to the uncertainties we consider melt water contents in the range 15–30 wt.% (Fei, 2021; Novella et al., 2017) and partial melt fractions in the range 0.1–1 wt.% (Fei, 2021; Schmandt et al., 2014) (see Text S5 for more details).

The predicted mineral and melt compositions for a pyrolitic bulk composition are shown in Fig. 3 (compo. A) as a function of f_{O_2}. The Fe contents of both melt and Brg that would be expected for a small degree melt in equilibrium with ultramafic lower mantle are lower than in this study and the Brg Al concentration is higher. Since the Brg $Fe^{3+}/\sum Fe$ ratio is positively dependent on its Al content and negatively dependent on the bulk Fe content (Huang et al., 2021), the $Fe^{3+}/\sum Fe$ ratio of Brg for a pyrolitic composition (compo. A) is calculated to be much higher than the experimental composition from this study (compo. B), at a comparable f_{O_2} (Fig. 3a). The melt $Fe^{3+}/\sum Fe$ ratio also changes slightly due to the different activity composition relations resulting from the use of Eq. (9), the terms of which are only known at 1 bar. The use of this relation, rather than ideal mixing, is justified, however, because as shown in Fig. 3b and d, this model reproduces the K_D (app) and $D_{\mathrm{Fe}}^{\mathrm{Brg/melt}}$ from Nakajima et al. (2019) when their bulk composition is employed (grey crosses in Fig. 3), even though these data were

not employed as part of the modeling. In contrast to the compositions in this study, quite a strong variation of K_D (app), $D_{Fe}^{Brg/melt}$ and $D_{Fe_2O_3}^{Brg/melt}$ with f_{O_2} is predicted for a pyrolitic bulk composition (Fig. 3b–d) whose Brg Fe/(Fe+Mg) ratio is lower. The uncertainties of the calculations arising from different melt fraction (0.1–1 wt.%) and water content (15–30 wt.%) assumptions are shown as shaded areas in Fig. 3. The potential range of uncertainty in melt fraction and water content has a minor influence on the $Fe^{3+}/\sum Fe$ ratio and K_D (app) between Brg and melt but would induce some variations of $D_{Fe}^{Brg/melt}$ and $D_{Fe_2O_3}^{Brg/melt}$ because the increase of melt H_2O content from 15 wt.% to 30 wt.% results in a decrease of all other melt components.

5. Discussion and implications

The increase in Brg $Fe^{3+}/\sum Fe$ ratio calculated for a pyrolitic compostion (compo. A in Fig. 3) compared to the experiments in this study (compo. B) is mainly a result of the higher Brg Al content. This means that although Fe^{3+} behaves moderately incompatibly in our experiment, with $D_{Fe_2O_3}^{Brg/melt} = 0.5(1)$, it becomes compatible in Brg upon partial melting of a pyrolitic composition, which also explains the differences in K_D (app) and $D_{Fe}^{Brg/melt}$ observed between this study and that of Nakajima et al. (2019). In Fig. 3 we also calculate K_D (app) for a slightly lower Brg Al content to show how strongly this affects K_D (app). The dependence of $D_{Fe}^{Brg/melt}$ on Brg Al content probably also explains similar differences in $D_{Fe}^{Brg/melt}$ observed between experiments performed with olivine and chondritic starting materials in the laser heated diamond anvil cell at pressures up to approxiamtly 120 GPa (Andrault et al., 2012; Nomura et al., 2011). Such effects and those resulting from changing f_{O_2} need to be understood in such experiments before more subtle effects can be ascribed to the occurrence of iron spin transitions. The $Fe^{3+}/\sum Fe$ ratio of both Brg and melt are expected to decrease to some extent with

342 temperature (Armstrong et al., 2019; Huang et al., 2021), however, if values of $D_{Fe_2O_3}^{Brg/melt}$>1
343 are maintained, the crystallization of Brg from a primordial magma ocean would have removed
344 ferric iron from the residual melt, resulting in solid lower mantle material with an initially
345 higher ferric iron content than the residual melt.

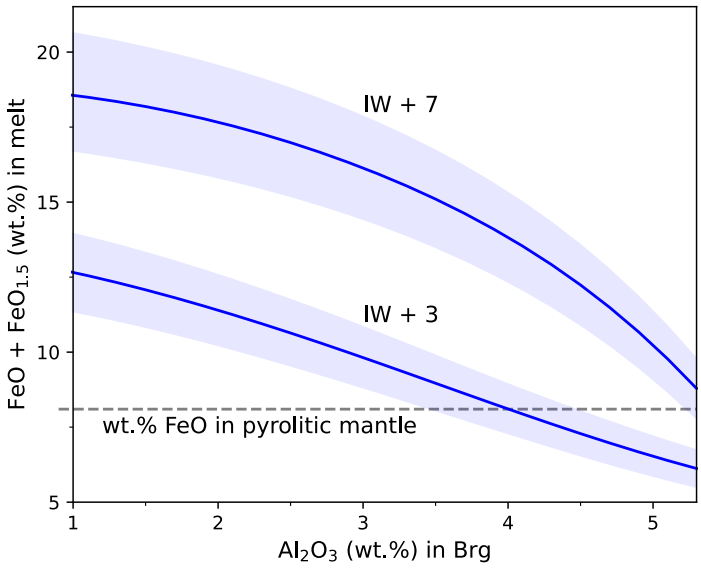

346

347 **Fig. 4.** The Fe content in hydrous melt versus the Al_2O_3 content in coexisting Brg calculated for a bulk
348 pyrolitic composition at a fixed f_{O_2} of IW + 3 or IW + 7 and a pressure of 25 GPa and temperature of
349 1973 K. The uncertainties caused by different assumptions of melt fractions and water contents are
350 shown by the shaded regions. The figure shows that the Fe content of hydrous melt is a strong function
351 of the Al content in Brg as well as the oxygen fugacity.

352 Using the iron content determined for partial melts at plausible f_{O_2} for the top of the lower
353 mantle, we can make an estimate of the corresponding melt density to examine whether they
354 could be neutrally buoyant and accumulate at these depths. If we consider a scenario
355 compatible with that proposed by Schmandt et al. (2014), then water that has accumulated in
356 the transition zone due to slab dehydration causes melting as the downwelling region enters the
357 lower mantle and the proportion of mineral hosted water drops (Palot et al., 2016; Panero et al.,
358 2020). If we assume that water is the dominant volatile component and carbon at these
359 conditions is hosted as diamond, then the f_{O_2} can be estimated through a simple C-O-H fluid

speciation calculation (Belonoshko & Saxena, 1991a; Belonoshko & Saxena, 1991b; Frost & McCammon, 2008) to be in the range between IW + 2 and IW + 4. Although we ignore melt as a component in this calculation it is unlikely to influence this range of fO_2 significantly. For a pyrolitic mantle the partial melt iron content is approximately 7(1) wt.%. Using the equations of state given in Text S6, the melt density is determined to be in a very narrow range between 3.81–3.83 g/cm^3 over the range of water content (15–30 wt.%), melt fraction (0.1–1 wt.%) and fO_2 (IW + 2 to + 4) employed in the calculation. This is within the range of melt densities proposed by Nakajima et al. (2019) and is much lower than the density of the surrounding lower mantle (~ 4.38 g/cm^3). It is, however, close to the density at the base of the transition zone (~ 3.99 g/cm^3), as constrained by the PREM model (Dziewonski & Anderson, 1981). As a consequence, the hydrous melts produced would rise out of the lower mantle, back into the transition zone and gradually crystalize as they lose water to the surrounding Rw. As proposed by Nakajima et al. (2019), if melting occurs in a region of downwelling, such as the south western USA where a downwelling rate of up to 2 cm/year is estimated (Schmandt et al., 2014), then the hydrous mantle will be continuously dragged down from the transition zone into the lower mantle. The observed low shear velocities could therefore arise due to melts continuously being formed and rising back into the transition zone, creating a melt layer that filters incompatible elements and strips them out of material entering the lower mantle.

From the current analysis for a pyrolitic mantle, the melt would not be expected to be particularly iron rich. However, as shown in Fig. 3b and Fig. 4 the melt iron content is strongly dependent on the Al content of Brg. If we consider that the downwelling mantle may have Al contents that vary due to variable levels of melt depletion, either from melting at ridges or at the sub arc mantle, then it is plausible that relatively high melt iron contents could be obtained. Similarly, the Al content of Brg will be lower near the 660 km discontinuity due to the presence of garnet (Irifune, 1994; Wood, 2000) and although we do not consider the effects of garnet on

melting, it probably does not lower the melt iron content in the same way as Brg because its ferric iron content is lower (McCammon & Ross, 2003). None the less, when we determine melt densities for a range of mantle Al contents (1.00–5.31 wt.% in Brg or 0.66–4.40 wt.% for the bulk composition) at IW + 3 (Fig. 4), the resulting range, 3.81–3.90 g/cm^3, is still lower than the residual lower mantle at these depths.

It is also interesting to note that in addition to being more iron-rich than the mineral assemblage at the top of the lower mantle, the rising partial melt would also have an (Mg+Fe)/Si ratio > 2.5 (Fig. 1a). The melt when it crystalizes due to water loss to Rw in the transition zone could crystallize Fp-rich material with iron contents which could range to values above those expected for the bulk lower mantle, particularly if many cycles of melting and crystallization had taken place. In this scenario water is the dominant volatile in the melt and carbon should be mainly present in diamond, because in the presence of sufficient H_2O, any carbon-bearing iron-metal is likely to be oxidized (Frost & McCammon, 2008; Wood et al., 1990). In a water dominated melt in equilibrium with diamond, carbon should still be present in the melt in a combination of redox neutral components, CO_2 and CH_4. A plausible mechanism for lithospheric diamond formation is that such redox neutral components form diamond upon cooling (Stachel & Luth, 2015). A similar mechanism may operate as water within partial melts from the lower mantle is lost to Rw as they enter the transition zone (Fig. 5). This would produce diamonds with a carbon isotope signature similar to that of the mantle as observed recently for proposed deep mantle diamonds (Regier et al., 2020). Furthermore, the crystallization of iron-rich Fp as these melts crystalize as a result of Rw hydration would be consistent with the nature of inclusions found in such diamonds (Kaminsky, 2012) as would the presence of H_2O-rich Rw inclusions (Pearson et al., 2014).

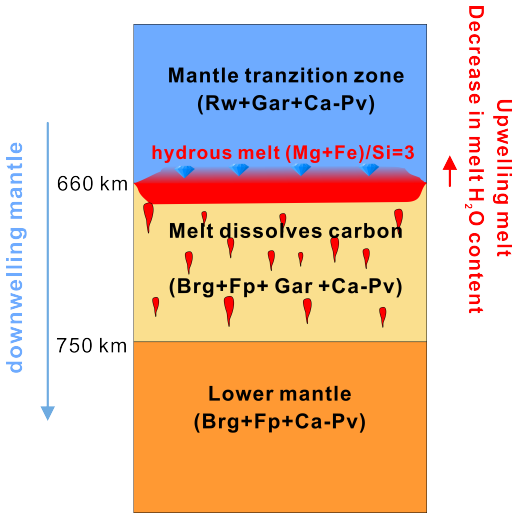

Fig. 5. Cartoon showing the downwelling of the mantle and the upwelling of the hydrous melt near the 660 discontinuity. When the downwelling region enters the lower mantle, the release of water due to the difference in water storage capacity between Brg and Rw would cause dehydration melting. From 660 km to 750 km depth, the Fe content in hydrous melt decreases from ~13 wt.% to ~6 wt.% as Brg Al content increases from 1 wt.% to 5 wt.% due to the transformation of garnet. The density of the hydrous melt is lower than the surrounding lower mantle. Melts should, therefore, rise back into the transition zone and freeze as H_2O from the melt partitions into Rw. Such melt may crystalize Fp due to their high (Mg+Fe)/Si ratio. The carbon components in the melt would crystalize to form diamond and may also trap hydrous Rw and Fp as inclusions. Rw: ringwoodite, Gar: garnet; Ca-Pv: calcium perovskite; Brg: bridgmanite; Fp: ferropericlase.

Acknowledgments

We would like to thank H. Fischer for high-pressure cell assembly machining, R. Njul for sample preparation and D. Krauße and A. Potzel for assistance with EPMA analysis. This work was supported by DFG grant FR1555/11.

References

Amundsen H.E.F., & Neumann, E.-R. (1992). Redox control during mantle/melt interaction. *Geochimica et Cosmochimica Acta, 56*, 2405-2416. https://doi.org/10.1016/0016-7037(92)90197-Q

Andrault D., Petitgirard, S., Lo Nigro, G., Devidal, J.-L., Veronesi, G., Garbarino, G., & Mezouar, M. (2012). Solid–liquid iron partitioning in Earth's deep mantle. *Nature, 487*, 354-357. https://doi.org/10.1038/nature11294

Armstrong K., Frost, D.J., McCammon, C.A., Rubie, D.C., & Ballaran, T.B. (2019). Deep magma ocean formation set the oxidation state of Earth's mantle. *Science, 365*, 903-906. https://doi.org/10.1126/science.aax8376

Belonoshko A., & Saxena, S.K. (1991a). A molecular dynamics study of the pressure-volume-temperature properties of super-critical fluids: I. H_2O. *Geochimica et Cosmochimica Acta, 55*, 381-387. https://doi.org/10.1016/0016-7037(91)90425-5

Belonoshko A., & Saxena, S.K. (1991b). A molecular dynamics study of the pressure-volume-temperature properties of supercritical fluids: II. CO_2, CH_4, CO, O_2, and H_2. *Geochimica et Cosmochimica Acta, 55*, 3191-3208. https://doi.org/10.1016/0016-7037(91)90483-L

Bercovici D., & Karato, S.-i. (2003). Whole-mantle convection and the transition-zone water filter. *Nature, 425*, 39-44. https://doi.org/10.1038/nature01918

Berryman J.G. (2000). Seismic velocity decrement ratios for regions of partial melt in the lower mantle. *Geophysical Research Letters, 27*, 421-424. https://doi.org/10.1029/1999GL008402

Bolfan-Casanova N., Keppler, H., & Rubie, D.C. (2000). Water partitioning between nominally anhydrous minerals in the $MgO–SiO_2–H_2O$ system up to 24 GPa: implications for the distribution of water in the Earth's mantle. *Earth and Planetary Science Letters, 182*, 209-221. https://doi.org/10.1016/S0012-821X(00)00244-2

Canil D., O'Neill, H.S.C., Pearson, D.G., Rudnick, R.L., McDonough, W.F., & Carswell, D.A. (1994). Ferric iron in peridotites and mantle oxidation states. *Earth and Planetary Science Letters, 123*, 205-220. https://doi.org/10.1016/0012-821X(94)90268-2

Corgne A., Liebske, C., Wood, B.J., Rubie, D.C., & Frost, D.J. (2005). Silicate perovskite-melt partitioning of trace elements and geochemical signature of a deep perovskitic reservoir. *Geochimica et Cosmochimica Acta, 69*, 485-496. https://doi.org/10.1016/j.gca.2004.06.041

Davis F.A., & Cottrell, E. (2018). Experimental investigation of basalt and peridotite oxybarometers: Implications for spinel thermodynamic models and Fe^{3+} compatibility during generation of upper mantle melts. *American Mineralogist, 103*, 1056-1067. https://doi.org/10.2138/am-2018-6280

Dziewonski A.M., & Anderson, D.L. (1981). Preliminary reference Earth model. *Physics of the Earth and Planetary Interiors, 25*, 297-356. https://doi.org/10.1016/0031-9201(81)90046-7

Fei H. (2021). Water content of the dehydration melting layer in the topmost lower mantle. *Geophysical Research Letters, 48*, e2020GL090973. https://doi.org/10.1029/2020GL090973

Frost D.J., & McCammon, C.A. (2008). The redox state of Earth's mantle. *Annual Review of Earth and Planetary Sciences, 36*, 389-420. https://doi.org/10.1146/annurev.earth.36.031207.124322

Garnero E.J., & McNamara, A.K. (2008). Structure and dynamics of Earth's lower mantle. *Science, 320*, 626-628. https://doi.org/10.1126/science.1148028

Garnero E.J., McNamara, A.K., & Shim, S.-H. (2016). Continent-sized anomalous zones with low seismic velocity at the base of Earth's mantle. *Nature geoscience, 9*, 481-489. https://doi.org/10.1038/ngeo2733

Hirose K., & Fei, Y. (2002). Subsolidus and melting phase relations of basaltic composition in the uppermost lower mantle. *Geochimica et Cosmochimica Acta, 66*, 2099-2108. https://doi.org/10.1016/S0016-7037(02)00847-5

Huang R., Boffa Ballaran, T., McCammon, C.A., Miyajima, N., Dolejš, D., & Frost, D.J. (2021). The composition and redox state of bridgmanite in the lower mantle as a function of oxygen fugacity. *Geochimica et Cosmochimica Acta, 303*, 110-136. https://doi.org/10.1016/j.gca.2021.02.036

Inoue T., Yurimoto, H., & Kudoh, Y. (1995). Hydrous modified spinel, $Mg_{1.75}SiH_{0.5}O_4$: a new water reservoir in the mantle transition region. *Geophysical Research Letters, 22*, 117-120. https://doi.org/10.1029/94gl02965

Irifune T. (1994). Absence of an aluminous phase in the upper part of the Earth's lower mantle. *Nature, 370*, 131–133. https://doi.org/10.1038/370131a0

Ito E., Kubo, A., Katsura, T., & Walter, M.J. (2004). Melting experiments of mantle materials under lower mantle conditions with implications for magma ocean differentiation. *Physics of the Earth and Planetary Interiors, 143-144*, 397-406. https://doi.org/10.1016/j.pepi.2003.09.016

Ito E., & Takahashi, E. (1987). Melting of peridotite at uppermost lower-mantle conditions. *Nature, 328*, 514-517. https://doi.org/10.1038/328514a0

Jayasuriya K.D., O'Neill, H.S.C., Berry, A.J., & Campbell, S.J. (2004). A Mössbauer study of the oxidation state of Fe in silicate melts. *American Mineralogist, 89*, 1597-1609. https://doi.org/10.2138/am-2004-11-1203

Kaminsky F. (2012). Mineralogy of the lower mantle: A review of 'super-deep' mineral inclusions in diamond. *Earth-Science Reviews, 110*, 127-147. https://doi.org/10.1016/j.earscirev.2011.10.005

Katsura T., Yoneda, A., Yamazaki, D., Yoshino, T., & Ito, E. (2010). Adiabatic temperature profile in the mantle. *Physics of the Earth and Planetary Interiors, 183*, 212-218. https://doi.org/10.1016/j.pepi.2010.07.001

Kawamoto T. (2004). Hydrous phase stability and partial melt chemistry in H_2O-saturated KLB-1 peridotite up to the uppermost lower mantle conditions. *Physics of the Earth and Planetary Interiors, 143*, 387-395. https://doi.org/10.1016/j.pepi.2003.06.003

Keppler H., & Frost, D.J. (2005). Introduction to minerals under extreme conditions. In Miletich, R. (Ed.), *Mineral Behaviour at Extreme Conditions, European Mineralogical Union Lecture Notes in Mineralogy* (Vol. 7, pp. 1-30). Budapest: Eötvös University Press. https://doi.org/10.1180/EMU-notes.7.1

Kohlstedt D.L., Keppler, H., & Rubie, D.C. (1996). Solubility of water in the alpha, beta and gamma phases of $(Mg,Fe)_2SiO_4$. *Contributions to Mineralogy and Petrology, 123*, 345-357. https://doi.org/10.1007/s004100050161

Kuwahara H., Nomura, R., Nakada, R., & Irifune, T. (2018). Simultaneous determination of melting phase relations of mantle peridotite and mid-ocean ridge basalt at the uppermost lower mantle conditions. *Physics of the Earth and Planetary Interiors, 284*, 36-50. https://doi.org/10.1016/j.pepi.2018.08.012

Lay T., Garnero, E.J., & Williams, Q. (2004). Partial melting in a thermo-chemical boundary layer at the base of the mantle. *Physics of the Earth and Planetary Interiors, 146*, 441-467. https://doi.org/10.1016/j.pepi.2004.04.004

Lay T., Williams, Q., & Garnero, E.J. (1998). The core–mantle boundary layer and deep Earth dynamics. *Nature, 392*, 461-468. https://doi.org/10.1038/33083

Liebske C., Corgne, A., Frost, D.J., Rubie, D.C., & Wood, B.J. (2005). Compositional effects on element partitioning between Mg-silicate perovskite and silicate melts. *Contributions to Mineralogy and Petrology, 149*, 113-128. https://doi.org/10.1007/s00410-004-0641-8

Liu Z., Park, J., & Karato, S.-i. (2016). Seismological detection of low - velocity anomalies surrounding the mantle transition zone in Japan subduction zone. *Geophysical Research Letters, 43*, 2480-2487. https://doi.org/10.1002/2015GL067097

Liu Z., Park, J., & Karato, S.-i. (2018). Seismic evidence for water transport out of the mantle transition zone beneath the European Alps. *Earth and Planetary Science Letters, 482*, 93-104. https://doi.org/10.1016/j.epsl.2017.10.054

Mallmann G., & O'Neill, H.S.C. (2009). The crystal/melt partitioning of V during mantle melting as a function of oxygen fugacity compared with some other elements (Al, P, Ca, Sc, Ti, Cr, Fe, Ga, Y, Zr and Nb). *Journal of Petrology, 50*, 1765-1794. https://doi.org/10.1093/petrology/egp053

McCammon C.A., Frost, D.J., Smyth, J.R., Laustsen, H.M.S., Kawamoto, T., Ross, N.L., & van Aken, P.A. (2004). Oxidation state of iron in hydrous mantle phases: implications for subduction and mantle oxygen fugacity. *Physics of the Earth and Planetary Interiors, 143*, 157-169. https://doi.org/10.1016/j.pepi.2003.08.009

McCammon C.A., & Ross, N.L. (2003). Crystal chemistry of ferric iron in (Mg,Fe)(Si,Al)O_3 majorite with implications for the transition zone. *Physics and Chemistry of Minerals, 30*, 206-216. https://doi.org/10.1007/s00269-003-0309-3

McFarlane E.A., Drake, M.J., & Rubie, D.C. (1994). Element partitioning between Mg-perovskite, magnesiowüstite, and silicate melt at conditions of the Earth's mantle. *Geochimica et Cosmochimica Acta, 58*, 5161-5172. https://doi.org/10.1016/0016-7037(94)90301-8

Murakami M., Hirose, K., Yurimoto, H., Nakashima, S., & Takafuji, N. (2002). Water in Earth's lower mantle. *Science, 295*, 1885-1887. https://doi.org/10.1126/science.1065998

Nakajima A., Sakamaki, T., Kawazoe, T., & Suzuki, A. (2019). Hydrous magnesium-rich magma genesis at the top of the lower mantle. *Scientific Reports, 9*, 7420. https://doi.org/10.1038/s41598-019-43949-2

Nakajima Y., Frost, D.J., & Rubie, D.C. (2012). Ferrous iron partitioning between magnesium silicate perovskite and ferropericlase and the composition of perovskite in the Earth's lower mantle. *Journal of Geophysical Research: Solid Earth, 117*, B08201. https://doi.org/10.1029/2012JB009151

Nomura R., Ozawa, H., Tateno, S., Hirose, K., Hernlund, J., Muto, S., et al. (2011). Spin crossover and iron-rich silicate melt in the Earth's deep mantle. *Nature, 473*, 199-202. https://doi.org/10.1038/nature09940

Novella D., Dolejš, D., Myhill, R., Pamato, M.G., Manthilake, G., & Frost, D.J. (2017). Melting phase relations in the systems Mg_2SiO_4–H_2O and $MgSiO_3$–H_2O and the formation of hydrous melts in the upper mantle. *Geochimica et Cosmochimica Acta, 204*, 68-82. https://doi.org/10.1016/j.gca.2016.12.042

Palot M., Jacobsen, S.D., Townsend, J.P., Nestola, F., Marquardt, K., Miyajima, N., et al. (2016). Evidence for H_2O-bearing fluids in the lower mantle from diamond inclusion. *Lithos, 265*, 237-243. https://doi.org/10.1016/j.lithos.2016.06.023

Panero W.R., Thomas, C., Myhill, R., Pigott, J.S., Raepsaet, C., & Bureau, H. (2020). Dehydration melting below the undersaturated transition zone. *Geochemistry, Geophysics, Geosystems, 21*, e2019GC008712. https://doi.org/10.1029/2019GC008712

Pearson D.G., Brenker, F.E., Nestola, F., McNeill, J., Nasdala, L., Hutchison, M.T., et al. (2014). Hydrous mantle transition zone indicated by ringwoodite included within diamond. *Nature, 507*, 221-224. https://doi.org/10.1038/nature13080

Regier M.E., Pearson, D.G., Stachel, T., Luth, R.W., Stern, R.A., & Harris, J.W. (2020). The lithospheric-to-lower-mantle carbon cycle recorded in superdeep diamonds. *Nature, 585*, 234-238. https://doi.org/10.1038/s41586-020-2676-z

Revenaugh J., & Meyer, R. (1997). Seismic evidence of partial melt within a possibly ubiquitous low-velocity layer at the base of the mantle. *Science, 277*, 670-673. https://doi.org/10.1126/science.277.5326.670

Rost S., Garnero, E.J., Williams, Q., & Manga, M. (2005). Seismological constraints on a possible plume root at the core–mantle boundary. *Nature, 435*, 666-669. https://doi.org/10.1038/nature03620

Schmandt B., Jacobsen, S.D., Becker, T.W., Liu, Z., & Dueker, K.G. (2014). Dehydration melting at the top of the lower mantle. *Science, 344*, 1265-1268. https://doi.org/10.1126/science.1253358

Smyth J.R., Holl, C.M., Frost, D.J., Jacobsen, S.D., Langenhorst, F., & McCammon, C.A. (2003). Structural systematics of hydrous ringwoodite and water in Earth's interior. *American Mineralogist, 88*, 1402-1407. https://doi.org/10.2138/am-2003-1001

Song T.R.A., Helmberger, D.V., & Grand, S.P. (2004). Low-velocity zone atop the 410-km seismic discontinuity in the northwestern United States. *Nature, 427*, 530-533. https://doi.org/10.1038/nature02231

Sorbadere F., Laurenz, V., Frost, D.J., Wenz, M., Rosenthal, A., McCammon, C., & Rivard, C. (2018). The behaviour of ferric iron during partial melting of peridotite. *Geochimica et Cosmochimica Acta, 239*, 235-254. https://doi.org/10.1016/j.gca.2018.07.019

Stachel T., & Luth, R.W. (2015). Diamond formation—Where, when and how? *Lithos, 220*, 200-220. https://doi.org/10.1016/j.lithos.2015.01.028

Stagno V., & Frost, D.J. (2010). Carbon speciation in the asthenosphere: Experimental measurements of the redox conditions at which carbonate-bearing melts coexist with graphite or diamond in peridotite assemblages. *Earth and Planetary Science Letters, 300*, 72-84. https://doi.org/10.1016/j.epsl.2010.09.038

Thorne M.S., & Garnero, E.J. (2004). Inferences on ultralow‐velocity zone structure from a global analysis of *SPdKS* waves. *Journal of Geophysical Research: Solid Earth, 109* https://doi.org/10.1029/2004JB003010

Toffelmier D.A., & Tyburczy, J.A. (2007). Electromagnetic detection of a 410-km-deep melt layer in the southwestern United States. *Nature, 447*, 991-994. https://doi.org/10.1038/nature05922

Trønnes R.G. (2000). Melting relations and major element partitioning in an oxidized bulk Earth model composition at 15–26 GPa. *Lithos, 53*, 233-245. https://doi.org/10.1016/S0024-4937(00)00027-X

Trønnes R.G., Canil, D., & Wei, K. (1992). Element partitioning between silicate minerals and coexisting melts at pressures of 1–27 GPa, and implications for mantle evolution. *Earth and Planetary Science Letters, 111*, 241-255. https://doi.org/10.1016/0012-821X(92)90182-U

Trønnes R.G., & Frost, D.J. (2002). Peridotite melting and mineral‐melt partitioning of major and minor elements at 22–24.5 GPa. *Earth and Planetary Science Letters, 197*, 117-131. https://doi.org/10.1016/S0012-821X(02)00466-1

Williams Q., & Garnero, E.J. (1996). Seismic evidence for partial melt at the base of Earth's mantle. *Science, 273*, 1528-1530. https://doi.org/10.1126/science.273.5281.1528

Williams Q., & Hemley, R.J. (2001). Hydrogen in the deep Earth. *Annual Review of Earth and Planetary Sciences, 29*, 365-418. https://doi.org/10.1146/annurev.earth.29.1.365

Wood B.J. (2000). Phase transformations and partitioning relations in peridotite under lower mantle conditions. *Earth and Planetary Science Letters, 174*, 341-354. https://doi.org/10.1016/S0012-821X(99)00273-3

Wood B.J., Bryndzia, L.T., & Johnson, K.E. (1990). Mantle oxidation state and its relationship to tectonic environment and fluid speciation. *Science, 248*, 337-345. https://doi.org/10.1126/science.248.4953.337